highest latitudes that can be seen (±60° to 75°) are always dark and featureless (2). These dark bands fall at the same latitudes as the "cold collar" seen at mid-infrared wavelengths (8 to 12 μm) (24–26). The cold collar has been attributed to a cold cloud top. Unlike the mid-infrared measurements, our NIR observations are not sensitive to the temperature of the cloud top. Instead, they indicate that the clouds have greater optical depths at these latitudes. The mechanisms that make the clouds more opaque and cloud tops colder at these latitudes are not currently known, but both phenomena could be produced by strong vertical convective mixing within the middle and upper cloud layers (49 to 57 and 58 to 65 km, respectively). This mixing would suspend larger cloud particles that are more opaque at NIR wavelengths. The almost adiabatic vertical temperature gradients derived from Pioneer Venus radio occultation observations at these altitudes and latitudes (27) appear to support this hypothesis.

The largest markings (>2000 km) at latitudes less than ±60°, including the planetary-scale dark cloud, the bright spot seen on 29 January and 10 February, and distinct features within the persistent mid-latitude bright bands (±40° to 60°) rotate from east to west in almost solid-body rotation with periods near 5.5 ± 0.15 days (Fig. 4). This corresponds to an equatorial velocity of 80 ± 3 m s^{-1} (17), which is about 10 m s^{-1} faster than that derived from earlier studies of NIR markings (1–3). Similar rotation periods were derived from markings tracked over both short (3- to 5-hour) and long (5- to 46-day) intervals. Unlike the largest markings, most small-scale (400 to 2000 km) markings at low latitudes had east-west velocities near 60 ± 7 m s^{-1}, indicating rotation periods near 7.4 ± 1 days. During the Galileo encounter, slow-moving, small-scale markings dominated the Venus night side at low latitudes (±30°), while faster moving large-scale features occupied higher latitudes.

The apparent coexistence of distinct rotation periods for large- and small-scale markings suggests that they are related to different phenomena. For example, they may provide independent estimates of the winds in the middle and lower cloud layers. To determine the plausibility of this hypothesis, we used the thermal wind equation (28) to estimate the north-south temperature gradient at 30° latitude implied by the observed velocity difference. If the faster component (75 m s^{-1}) was centered near 0.6 bar (middle cloud) and the slower component (60 m s^{-1}) was centered near 1.3 bars (lower cloud), the computed poleward temperature gradient is −0.14 K per degree of latitude. Measurements by the Pioneer Venus entry probes (29) and radio occultation experiment (27) reveal similar horizontal temperature gradients near the 1-bar (50 km) level and support this interpretation of the distinct NIR marking velocity profiles.

REFERENCES AND NOTES

1. D. A. Allen and J. W. Crawford, *Nature* **307**, 222 (1984).
2. D. Crisp *et al.*, *Science* **246**, 506 (1989).
3. D. A. Allen, *Icarus* **69**, 221 (1986).
4. L. W. Kamp, F. W. Taylor, S. B. Calcutt, *Nature* **336**, 360 (1988).
5. L. W. Kamp and F. W. Taylor, *Icarus* **86**, 510 (1990).
6. B. Bezard *et al.*, *Nature* **345**, 508 (1990).
7. J. H. Hoffman *et al.*, *J. Geophys. Res.* **85**, 7882 (1980).
8. V. I. Oyama *et al.*, *ibid.*, p. 7891.
9. V. I. Moroz, in *Venus*, D. M. Hunten, L. Colin, T. M. Donahue, V. I. Moroz, Eds. (Univ. of Arizona Press, Tucson, 1983), pp. 45–68.
10. C. DeBergh *et al.*, *Science* **251**, 547 (1991).
11. J. F. Bell III *et al.*, *Bull. Am. Astron. Soc.* **22**, 1052 (1990).
12. J. F. Bell III *et al.*, *Science* **252**, 1293 (1991).
13. R. Carlson *et al.*, *ibid.* **253**, 1541 (1991).
14. D. Allen, *Int. Astron. Union Circ.* 4962 (1990); D. Crisp *et al.*, *Bull. Am. Astron. Soc.* **22**, 1053 (1990).
15. D. Crisp *et al.*, *Science* **253**, 1263.
16. In January, images were taken from Cerro Tololo and Kitt Peak. In February, images were taken from Las Campanas, Kitt Peak, Palomar, Mauna Kea, and the Anglo-Australian Observatory.
17. Three different methods were used to track NIR markings. In the first, maps created from images taken at different times were displayed and the latitudes and longitudes of common markings were recorded. Displacements of markings were converted to distances and we computed velocities by dividing these values by the elapsed time. In the second method, a single map was displayed, and we selected a specific marking by surrounding it with a box. We located this feature on subsequent maps by translating the maps in latitude and longitude until the mean contrast and root-mean-square intensity difference within the chosen box were minimized. The last method was a completely automated version of the second, which used the brightness variance within specified latitude-longitude bins to track distinct markings.
18. D. Crisp, *Icarus* **77**, 391 (1989).
19. V. M. Linkin *et al.*, *Science* **231**, 1420 (1986).
20. D. Crisp *et al.*, *Adv. Space Res.* **10**, 109 (1990).
21. C. C. Counselman *et al.*, *J. Geophys. Res.* **85**, 8026 (1980).
22. H. E. Revercombe *et al.*, *Icarus* **61**, 521 (1985).
23. S. S. Limaye, *Adv. Space Res.* **5**, 51 (1985).
24. D. Diner *et al.*, *Icarus* **27**, 191 (1976); D. Diner *et al.*, *ibid.* **52**, 301 (1982).
25. F. W. Taylor *et al.*, *J. Geophys. Res.* **85**, 7963 (1980).
26. G. S. Orton, J. Caldwell, A. J. Friedson, T. Z. Martin, *Science* **253**, 1536 (1991).
27. A. J. Kliore and I. R. Patel, *J. Geophys. Res.* **85**, 7957 (1980).
28. C. B. Leovy, *J. Atmos. Sci.* **30**, 1217 (1973).
29. A. Seiff, *J. Geophys. Res.* **85**, 7903 (1980).

30. This work was funded in part by grants from the NASA Planetary Astronomy and Planetary Atmospheres Programs to the Jet Propulsion Laboratory (JPL), California Institute of Technology, and the NASA Ames Research Center. Additional support for S. McMuldroch was provided by the Science and Engineering Research Council. Computer time was provided by the Wide-Field/Planetary Camera II Project at JPL. Contribution 5067 from the Division of Geological and Planetary Sciences, California Institute of Technology.

3 April 1991; accepted 17 July 1991

Galileo Infrared Imaging Spectroscopy Measurements at Venus

R. W. CARLSON, K. H. BAINES, TH. ENCRENAZ, F. W. TAYLOR, P. DROSSART, L. W. KAMP, J. B. POLLACK, E. LELLOUCH, A. D. COLLARD, S. B. CALCUTT, D. GRINSPOON,* P. R. WEISSMAN, W. D. SMYTHE, A. C. OCAMPO, G. E. DANIELSON, F. P. FANALE, T. V. JOHNSON, H. H. KIEFFER, D. L. MATSON, T. B. MCCORD, L. A. SODERBLOM

During the 1990 Galileo Venus flyby, the Near Infrared Mapping Spectrometer investigated the night-side atmosphere of Venus in the spectral range 0.7 to 5.2 micrometers. Multispectral images at high spatial resolution indicate substantial cloud opacity variations in the lower cloud levels, centered at 50 kilometers altitude. Zonal and meridional winds were derived for this level and are consistent with motion of the upper branch of a Hadley cell. Northern and southern hemisphere clouds appear to be markedly different. Spectral profiles were used to derive lower atmosphere abundances of water vapor and other species.

THE FEBRUARY 1990 GALILEO FLYBY provided a unique opportunity to investigate the clouds, motions, and deep-atmosphere composition of Venus with infrared imaging spectrscopy. The spectral range and spatial resolution of the

R. W. Carlson, K. H. Baines, L. W. Kamp, P. R. Weissman, W. D. Smythe, A. C. Ocampo, T. V. Johnson, D. L. Matson, Jet Propulsion Laboratory, California Institute of Technology, Pasadena, CA 91109.
Th. Encrenaz, P. Drossart, E. Lellouch, Observatoire de Paris, F-92195 Meudon, France.
F. W. Taylor, A. D. Collard, S. B. Calcutt, Oxford University, Oxford OX1 3PU, United Kingdom.
J. B. Pollack and D. Grinspoon, National Aeronautics and Space Administration (NASA) Ames Research Center Moffett Field, CA 94035.
G. E. Danielson, Division of Geological and Planetary Sciences, California Institute of Technology, Pasadena, CA 91109.
F. P. Fanale and T. B. McCord, University of Hawaii, Honolulu, HI 96822.
H. H. Kieffer and L. A. Soderblom, U.S. Geological Survey, Flagstaff, AZ 86001.

*Present address: University of Colorado, Boulder, CO 80309.

Galileo Near Infrared Mapping Spectrometer (NIMS) experiment, although specifically designed for Jupiter measurements, were fortuitously capable of investigating recently discovered atmospheric emission features on Venus, which occur in the region from 1 to 2.8 μm (*1, 2*) and arise from surface and deep atmosphere thermal emission (*3–5*). These emissions, weak as compared to reflected solar radiation, are discernible on the unilluminated (night) side of Venus and occur in windows of relative gaseous spectral transparency. The spectral shape of these features, influenced by absorption by minor species, as well as CO_2, can be used to perform compositional sounding of the lower atmosphere (*2–4, 6*). In addition, the radiation emanating from below is modulated by spatial and temporal variations in the intervening cloud layers, providing a means to study Cytherian cloud properties and their motions. Furthermore, at longer wavelengths (>~2.8 μm), the NIMS can be used to study the clouds and upper atmosphere by measuring cloud and upper atmosphere thermal emission. Thus, the NIMS experiment allows one to probe the Venus atmosphere from near the surface to an altitude of ~100 km.

The NIMS instrument (*7*) is an imaging spectrometer, consisting of a telescope, a diffraction grating spectrometer, and 17 individual photodiode detectors that are radiatively cooled to ~65 K. This combination of detectors (2 Si, 15 InSb) and grating positions (24) covers the spectral range from 0.7 to 5.2 μm, with a spectral resolution of 0.013 (0.026) μm for wavelengths less (greater) than 1 μm. NIMS is a "pushbroom" imager, with one dimension of spatial scanning performed by mirror scanning within the instrument, yielding a linear image 20 pixels (10 mrad) in height; the orthogonal dimension is scanned through spacecraft scan-platform motion, generating swaths that are mosaicked to form larger images. The angular resolution is 0.5 mrad, yielding center-of-disk pixel sizes of 11 to 50 km for our Venus night-side measurements.

Two different types of observations were used for the measurements reported here. In the first case, we obtained multispectral images using a mode for which the grating is fixed and images are simultaneously obtained at 17 different wavelengths (indicated in Fig. 1). Two such sets of multispectral images were obtained as Galileo approached Venus, and the time difference between these image sets allowed cloud motions to be determined. These two image sets, termed VPDIN-1 and VPDIN-2, were obtained at ~50 and ~11 to ~22 km pixel^{-1}, respectively, and provide much better spatial resolution than that obtainable from ground-based observations.

In the second case, VJBARS, spatial coverage was reduced in order to obtain comprehensive spectral coverage, and complete spectra with 408 spectral elements were obtained from ~500 locations on the disk. These were generally oriented in lines along the subspacecraft meridian and were ~25 km in pixel size.

During our night-side measurements, the instrument viewed through angles that included the spinning sections of the spacecraft. This portion of the spacecraft contains several appendages that periodically obscure the NIMS field of view during its ~20-s spin period. In order to minimize the amount of obscured data, all spatial and spectral measurements were multiply sampled, yielding more than 90% unobscured data. We identified obscured measurements by subsequently mapping the spinning portion of the spacecraft using NIMS itself, identifying the locations of obscuring elements and using these results to flag any questionable data, retaining only valid, unobscured measurements.

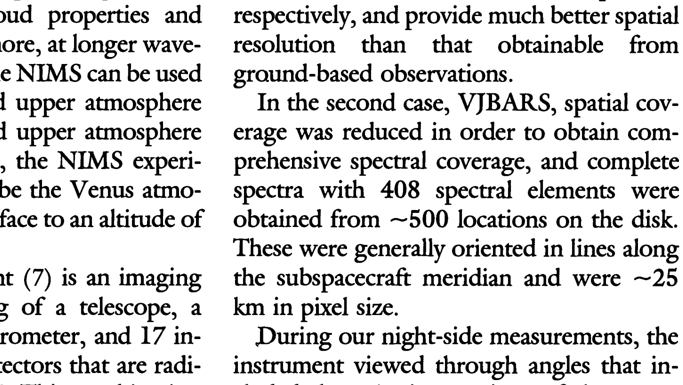

Fig. 1. A representative NIMS spectrum of the dark side of Venus. This spectrum was obtained near the center of the disk during the VJBARS sequence and shows two different spectral regimes. In the long-wavelength region (λ > ~2.8 μm) the Venus sulfuric acid clouds are highly absorbing, and the observed radiation is generally due to cloud thermal emission, radiating at a brightness temperature of ~235 K. Several CO_2 absorption bands are identified. In these bands, the central intensities are reduced and are due to thermal emission produced in the higher and colder atmosphere. For shorter wavelengths (λ < ~2.8 μm), the clouds are more transparent, allowing one to sense thermal radiation that is produced in the deep atmosphere, well below the cloud layer. In spectral regions where gaseous absorption is low, thermal radiation emitted in the lower and hotter atmosphere can escape and produce the spectral features seen in the figure. A portion of the λ <1 μm intensities is due to instrumentally scattered light originating from the bright sunlit crescent. The locations of the FIXED MAP wavelengths used in the VPDIN-1,2 images are shown as vertical lines.

An average spectrum obtained near the center of the disk during the VJBARS sequence is shown in Fig. 1. In the shorter wavelength region we observed the 1.74- and 2.30-μm features, originally discovered by Allen (*1*), as well as recently discovered features at 1.09, 1.18, 1.27, and 1.30 μm (*2*). We also found a new feature at 1.01 μm. The spectrum below ~2 μm shows weak contamination by instrumentally scattered light emanating from the nearby bright crescent. However, a portion of this radiation, at least at 0.80 μm, must be due to atmospheric emissions from Venus because the dark-side limb is clearly evident in the 0.8-μm imagery data, albeit weak. On the basis of theoretical calculations (*3*) and near-infrared transmission measurements of the Venus atmosphere by Venera 11 (*8*), it is reasonable to expect emission features to be present for wavelengths shortward of ~0.9 μm.

At wavelengths longer than ~2.8 μm, a different spectral regime is apparent in which thermal radiation is seen from both the clouds and, in regions of CO_2 absorption, from the overlying atmosphere. The wavelengths used for the VPDIN-1,2 maps (discussed below) are indicated in Fig. 1 and show that these images pertain to a variety of spectral regimes and altitudes.

The two multispectral image data sets (VPDIN-1,2) are shown in Figs. 2 and 3 for selected wavelengths, along with a reference grid and topographic map (Fig. 2E). To best visualize the spatial structure in the images, a fill algorithm was used to cosmetically correct obscured data. Images for 1.18 and 1.74 μm, not shown, depict a cloud opacity structure similar to the 2.30-μm image (Fig. 2A) but their contrast is less than that of the 2.30-μm case, where contrasts of 20:1 are observed. Equivalent intensity contrast ratios for 1.74- and 1.18-μm images are ~5:1 and 2:1, respectively. Another difference between the 2.30- and 1.18-μm images is the presence of a weak 1.18-μm intensity depression seen in both VPDIN-1 and VPDIN-2 images. This feature coincides, within pointing uncertainties, with the location of Maxwell Montes, and the intensity isophotes exhibit the same shape as the topography of Maxwell Montes (*9*). These observations indicate that high-altitude (~10 km) surfaces can influence the short-wavelength flux, as would be expected from the radar-measured height of Maxwell, which implies, if we assume an adiabatic lapse rate, contrasts of the order observed.

The 2.30-μm image (Fig. 2A) shows disorganized structure in the equatorial region, suggestive perhaps of turbulent processes. For high northern and southern latitudes, linear features are seen that are inclined to lines of constant latitude. If these are interpreted as streamlines, then poleward meridional transport (such as Hadley cell circulation) is suggested. The northern polar vortex is seen at ~60°N. The north polar cap is quite dark, with virtually no radiated flux evident at 1.18, 1.74, or 2.30 μm, indicating the presence of a very thick cloud in the north polar region.

Thermal emission from the clouds is illustrated in Fig. 2, B and C, corresponding to wavelengths of 3.71 and 4.56 μm, respectively. Aside from limb darkening and the cold polar collar, the only other obvious features appear to be two linear markings in the northern hemisphere, some diffuse equatorial structure, and a cold band in the low southern hemisphere. There is very little contrast in these images. For example, the lower of the two "bright" hemisphere features seen in the 3.71-μm image is less than 20% brighter than the center-of-disk value. There appears to be little correlation between these thermal emission maps (Figs. 2, B and C) and the 2.30-μm cloud opacity map (Fig. 2A).

A higher altitude regime is depicted in Fig. 2D, which shows thermal emission within a strong CO_2 band (the $\nu_1 + \nu_2$ band at 4.84 μm). At this wavelength, the absorption cross section is sufficiently strong that vertical sounding probes altitudes several kilometers above the cloud tops. The high-altitude warm polar cap (*10*) is clearly evident (shown in red), and the quasi-isothermal region above the polar collar (*10*) is also seen. The cold band in the southern hemisphere seems to persist between this image and the preceding two images (Fig. 2, B and C).

Images at 1.18, 1.74, and 2.30 μm (see Fig. 2A) arise from thermal radiation emanating from below the cloud layers (*11*) and are modulated by spatial and temporal opacity variations in the intervening clouds. One of the striking features of these data is the large intensity variation at 2.30 μm, where we observe contrasts of up to 20:1. The optical depth of the cloud at visible wavelengths is ~25 to 40, and Mie scattering calculations indicate similar optical depths for near-infrared wavelengths. Radiative transfer calculations indicate that, in order to produce intensity changes of 20:1, the cloud opacity changes from ~34 to ~45 at 2.30 μm; that is, bright areas correspond to a 25% decrease in cloud number density or extinction cross section, or both, as compared to nearby dark areas.

Although extreme variations are observed at 2.30 μm, there is little spatial variation in the 3- to 5-μm images, and any variations that do appear exhibit little correlation with shorter wavelength images (compare Fig. 2A with Fig. 2, B and C). The longer wavelength radiation (for $\lambda = 3.71$ and 4.84 μm, Fig. 2, B and C) originates from cloud thermal emission, with contribution from the entire cloud but mainly from the upper portions. The extreme changes in opacity noted above for the 2.30-μm case must occur well below the cloud top, otherwise there would be more variation in the long-wavelength thermal-emission pattern of the cloud than is observed. One can constrain the altitude range that produces the contrast at 2.30 μm by comparing the observations with numerical calculations, relating the intensity variations for given wavelengths to cloud changes in given altitude regions. The data show that a factor of 10 change in the 2.30-μm intensity corresponds to less than a 10% change in the 3.71-μm radiance, with lesser variation for other long-wavelength channels. Numerical calculations show that substantial changes in the 2.30-μm radiance, which do not significantly affect the longer wavelength intensities, occur as a result of alterations in the bottom cloud region, specifically only the first few kilometers above the cloud base. In particular, relating the intensity changes observed in the VPDIN-1 images at 2.30 and 3.71 μm shows that the brightness temperature (at 3.71 μm) varies by ~0.13 K per unit change in cloud optical depth. From numerical simulations, the corresponding value would be ~1, 0.3, or 0.01 if the cloud changes occurred in altitude regions from 54 to 57, 50 to 54, or 48 to 50 km, respectively. Thus, the observed opacity changes must occur between 48 km (the bottom of the Venus cloud deck) and roughly 52 km, with a mean altitude of ~50 km. If the total cloud opacity changes by 25%, and this only occurs in the lowest few kilometers of the clouds [itself contributing ~25% to the total opac-

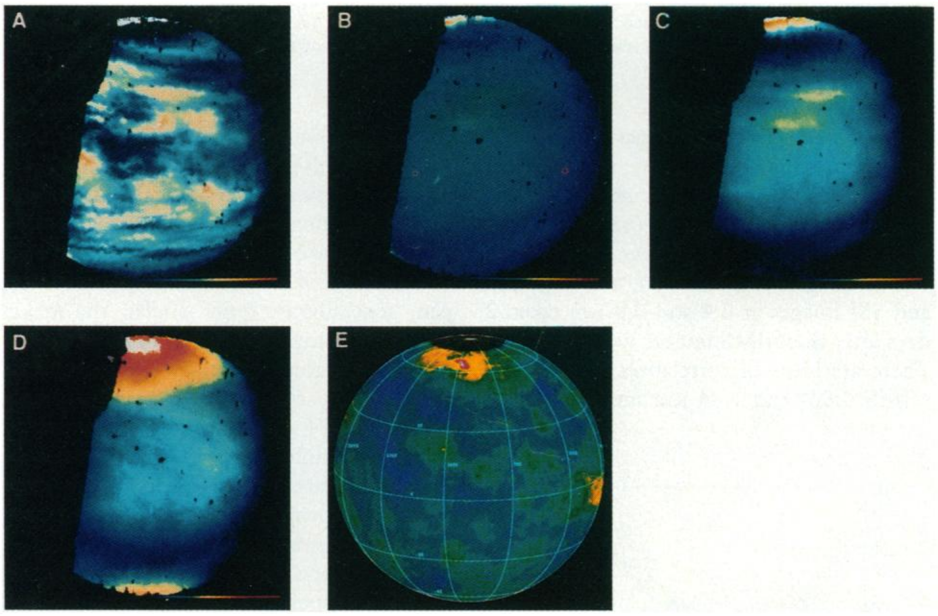

Fig. 2. Multispectral images of the night side of Venus. These data were obtained during the first NIMS imaging sequence (VPDIN-1) at a resolution of ~50 km pixel^{-1} (see Table 1). The FIXED MAP mode was used, wherein 17 different wavelengths are imaged simultaneously, and a few of these are illustrated here (A–D), along with a reference grid and topographic map (E). An orthographic projection was used, which is similar to the view seen by the Galileo spacecraft. The planet and atmosphere rotate from right to left. We have cosmetically corrected these images by filling in most of the ~9% obscured pixels, using the values of nearby pixels. A portion of the sunlit crescent is visible at the top of the images. (**A**) The 2.30-μm map, for which the radiation emanates from lower atmosphere thermal emission and is modulated by spatial variations in the clouds, with bright areas indicating thinner clouds. (**B**) A highly stretched image at a wavelength of 3.71 μm. This radiation arises from cloud thermal emission with a brightness temperature of 235 K. The actual intensity contrast at this wavelength is very slight, and this constancy can be used to constrain the vertical location of the cloud variations seen at 2.30 μm (see text). (**C**) An image corresponding to 4.56-μm wavelength, which is also produced by cloud thermal emission. Structure similar to that at 3.71 μm is evident, but the intensity contrast found here is somewhat greater. (**D**) An image at 4.84 μm, which is within a CO_2 combination band ($\nu_1 + \nu_2$); this radiation arises from upper atmosphere thermal emission, with a mean emission level occurring several kilometers above the cloud level. (**E**) A reference grid combined with a Pioneer Venus topographic map (*9*). The Venus prime meridian (0° longitude) is just left of the central meridian. Maxwell Montes, at ~64°N, 2.7°E, is in the north, center. Images at 1.18 μm (not shown) suggest an influence from this high-altitude (10 km) feature.

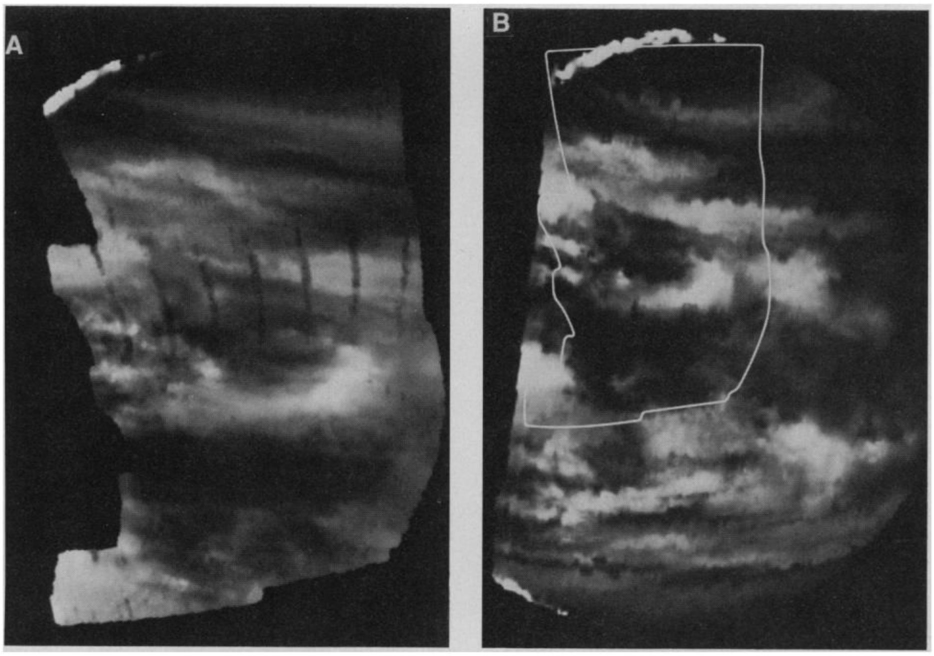

Fig. 3. (**A**) A high spatial resolution image of the northern hemisphere of Venus obtained at 2.30 μm during the VPDIN-2 sequence, at a resolution (referred to the nadir) varying from 22 km (top) to 11 km (bottom). The region mapped in this image is outlined in the corresponding VPDIN-1 image (**B**) and includes the bright crescent (upper left). Vertical striping in the upper middle, bottom left, and elsewhere in (A) is due to spacecraft obscuration. Such imagery (A and B), obtained with a time separation of ~2 hours, can be used to investigate wind velocities at the ~50-km level.

ity (*10*)], then extreme changes in this lower region are indicated.

In collaboration with A. Ingersoll and the Galileo Solid State Imaging (SSI) Team, we have searched for correlation between the NIMS images at 2.30, 4.56, and 4.84 μm and SSI images at 0.4 and 0.9 μm taken 2 days after the NIMS images were obtained. There are hints of correlation between the NIMS 4.56- and 4.84-μm images and the

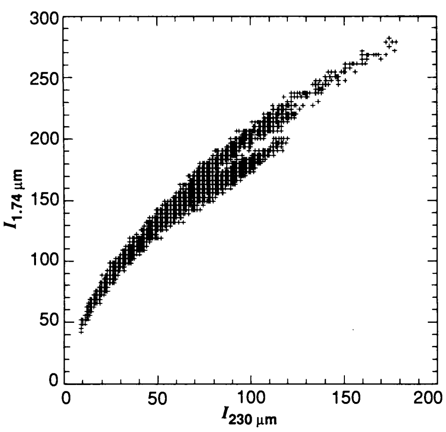

Fig. 4. Intensity scatter plots that relate the VPDIN-1 radiances at 2.30 and 1.74 μm. Intensities are in units of erg s^{-1} cm^{-2} $ster^{-1}$ μm^{-1}. We show data for the central area of Fig. 2, corresponding to emission angles less than ~40°. Two distinct branches, suggesting different cloud types, are indicated in these data, a trend that persists over the entire data set.

SSI 0.9-μm images, that is, linear features running north-south, but the possibility of misidentification of features dissuades us from estimating velocities or altitudes.

The cloud opacity images, obtained at wavelengths of λ = 1.18, 1.74, and 2.30 μm, generally are quite similar, the major difference being the contrast between bright and dark features. However, upon closer examination, comparison of the radiances at 2.30 and 1.74 μm shows that there appear to be two different and distinct types of clouds, indicated by the development of two branches shown in Fig. 4. We generated a map that distinguishes the two different cloud types and shows their spatial distribution. The upper (lower) branch of Fig. 4 is represented in red (blue) in the map of Fig. 5, which shows clear hemispherical differences, along with probable banded structure in the northern hemisphere, perhaps associated with a high-speed zonal jet observed at ~45°N (see below). An emission angle effect is absent, except near the limbs. The cause of these differing cloud types is unknown; it could be due to lower atmospheric temperature or gas opacity differences, although this seems unlikely on the basis of the uniform temperature and pressure measurements obtained by the Pioneer and Venera probes (*12*). Another mechanism could be physical differences in the clouds, with correspondingly different radiative transfer characteristics.

From the movement of individual clouds observed in the two Venus mapping sequences (VPDIN-1 and VPDIN-2), we have measured the zonal and meridional wind profiles for the northern hemisphere 50-km level (see Fig. 6); observations at both 1.74 and 2.30 μm were used. No systematic differences in cloud movements were observed between the two wavelengths. In all, 84 individual points were observed between the two wavelengths. All these points lie between the equator and 60°N and were tracked over the approximate 2-hour interval between the two Venus mapping sequences. The errors due to finite spatial resolution are estimated to be 1 pixel (~50 km for VPDIN-1) over the ~2-hour time difference, or ~6 m s^{-1}. We have used spacecraft-supplied pointing information, slightly corrected by limb-fitting. The systematic errors for these geometric corrections correspond to approximately 3 m s^{-1}. It is likely that much of the dispersion described by the error bars is due to true variations in the wind velocity.

We noted above that cloud variations occur in the bottom levels of the Venus clouds, with an average altitude of ~50 km. The dominant motion that we find in this region, similar to that known for the upper-cloud region (*13*), is a retrograde zonal rotation, with the wind direction nearly due west (see Fig. 6A). This is consistent with localized measurements by the Pioneer probes (*14*) and the Vega balloons (*15*). From equatorial through tropical latitudes,

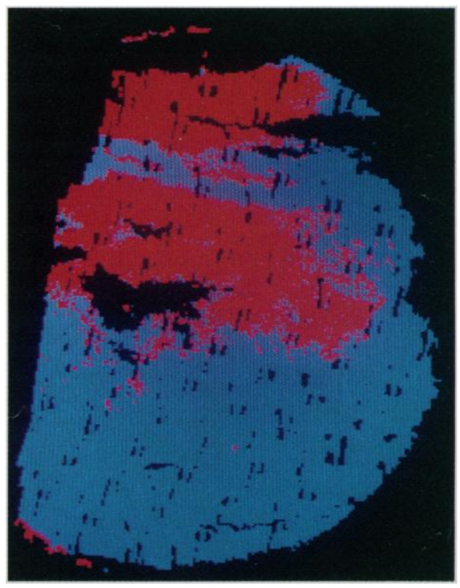

Fig. 5. A map of the two different cloud types, corresponding to the two branches indicated in Fig. 4. The upper branch of Fig. 4 is shown in red, the lower branch in blue. Low-intensity areas, for which the distinction is uncertain, are shown as dark areas. A hemispherical difference is seen, and a linear feature at ~45°N is suggested.

the zonal components of the wind vectors are relatively uniform, with the mean zonal flows varying from 53 m s^{-1} (at 5°N) to 63 m s^{-1} (at 35°N). Northward of 35° the winds become significantly stronger, increasing to a maximum of about 100 m s^{-1} at about 45°N, although this velocity value is quite imprecise. This mid-latitude jet extends over 1000 km in width (that is, 10° latitudinal extent), and exhibits a rotation period of ~3 to 4 days, a rate that is almost twice that observed at lower latitudes. The observed low-latitude zonal wind speed is in agreement with that obtained nearly simultaneously from ground-based measurements (*16*). It is somewhat less than the velocities measured at similar subsolar longitudes by the Vega balloons (*15*). However, the balloon measurements refer to a somewhat higher altitude, and vertical shear could account for the differences. Our measurement near 55°N of 73 ± 11 m s^{-1} agrees well with the Pioneer North Probe's measurement (58°N, the only dark-side probe measurement obtained at comparable altitudes in the hemisphere viewed by NIMS) of some 70 m s^{-1}, reported by Counselman *et al.* (*14*), suggesting temporal stability in the zonal winds at high latitudes.

The meridional wind component (see Fig. 6B) is approximately an order of magnitude less than the zonal component. Given the relatively large (6 m s^{-1}) uncertainty in individual wind measurements, poleward-directed winds are consistent with the data, although the mean wind speed measured within the 27.5° ± 2.5° bin is slightly equatorward. A generally poleward-directed wind is consistent with the Vega-1 balloon measurement at 7.1°N, although our near-equatorial wind of 6.5 ± 4.5 m s^{-1} is substantially larger than the Vega determination of 0.2 ± 1.3 m s^{-1} measured by Crisp *et al.* (*15*). Nevertheless, the overall poleward character of the meridional circulation in the northern hemisphere is apparent and is similar to that measured for the upper level winds by earlier ground-based and spacecraft experiments (*13*). Southern hemisphere features, if interpreted as streamlines, also indicate poleward flow, in this case toward the southern polar region, as expected for the upper path of a Hadley cell. Consequently, the 50-km region does not represent the bottom, or return path, of an upper level Hadley cell. The return, equatorward, flow probably lies below the 50-km level, although one cannot rule out the possibility that the 50-km region represents a different Hadley cell than is observed in ultraviolet images, in which case the upper level cell is constrained to be above the 50-km level that is observed in our measurements (*17*).

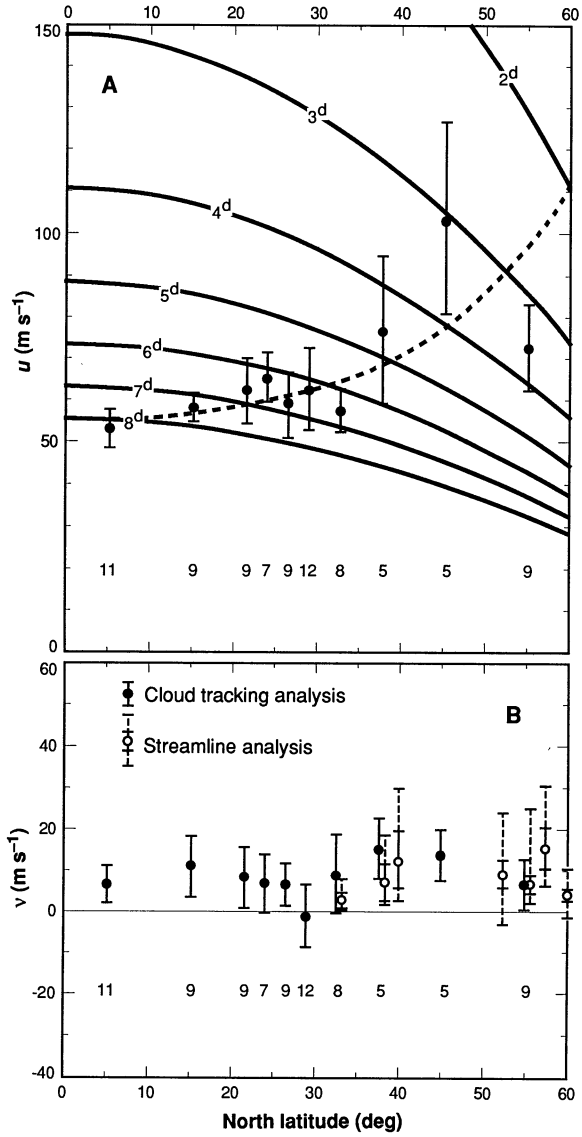

Fig. 6. (**A**) Zonal wind velocities for the ~50-km level in the northern, dark-side hemisphere. Mean zonal winds over 10° latitude bins (for θ < 20 and θ > 40), 2.5° bins (for 20 < θ < 30), and 5.0° bins (for 30 < θ < 40) are depicted (filled circles). Vertical bars depict the 1σ dispersion found within these bins. Uncertainty in the wind measurement for an individual speed determination due to operator measurement and finite pixel resolution are estimated to be ~6 m s^{-1}. This is less than the observed dispersion, suggesting that true variations in the wind speed are observed. The number of data points used in each bin is listed below each vertical bar. Systematic zonal velocity error due to uncertainty in the geometric registration is 3.2 m s^{-1} and is not included within the dispersion bars. Solid lines denote the atmospheric rotation period implied by the zonal wind speed, in Earth days; the dashed curve represents constant angular momentum for an equatorial velocity of 55 m s^{-1}. Uniform zonal velocities are observed in equatorial and middle latitudes, with a jetlike feature suggested at ~45°N. (**B**) Meridional wind speeds. These wind speeds are similarly for northern hemisphere, dark-side observations. Mean meridional winds are depicted (filled circles), based on observed cloud movements and using the same binning as in (A). Systematic error due to uncertainty in the geometric registration of the maps is 2.1 m s^{-1} and is not included within the dispersion bars. Also shown are mean winds (open circles) derived from the slopes of linear features, assuming that these features are streamlines and using the zonal wind profile shown in (A). In this streamline analysis, uncertainties in mean meridional winds due to zonal wind dispersions are depicted (solid vertical bar). Dashed vertical bars denote the range of meridional winds implied by the range of latitude versus longitude slopes observed for features in that latitude range.

We have used our zonal and meridional feature-tracking results to compute air-mass trajectories, attempting to compare these models with the observed streamline patterns shown in Fig. 2A. Specifically, following a similar analysis by Schinder *et al.* (*18*), we have compared in Fig. 7 the measured meridional winds to those based on the measured zonal winds and the longitude versus latitude slopes, α, of prominent linear cloud features observed at middle and polar latitudes. We utilize the equation $\nu(\theta) = \alpha[u(\theta) - u(0)\cos\theta]/\cos\theta$, where $u(\theta)$ is the measured zonal component at latitude θ. We find that the orientation of linear cloud features observed at middle and polar latitudes is consistent with predicted streamlines traversed by moving air parcels. Figure 7 shows computed particle trajectories in a reference frame that corotates with the equatorial winds. Near the equator, particles move predominantly poleward in this reference frame at a few meters per second. Near mid-latitudes, the particle motion accelerates significantly and turns westerly, as a result of the prominent departure there of the mean flow from the solid-body rotation. The orientations of linear cloud features observed at temperate and polar latitudes mimic the directions of theoretical particle paths.

Spectral features observed in CO_2 windows include absorptions attributable to bands of water vapor, CO, OCS, and possibly SO_2 and HCl, as well as additional weak bands of CO_2. One can therefore retrieve information on the abundances (and to some extent, the vertical distribution) of

Fig. 7. Particle streamline trajectories predicted by the mean zonal and meridional winds derived from cloud motion studies. Tick marks are in 1000-min (16.666-hour) increments. The theoretical stream functions are consistent with the orientation of linear cloud features observed at temperate and polar latitudes.

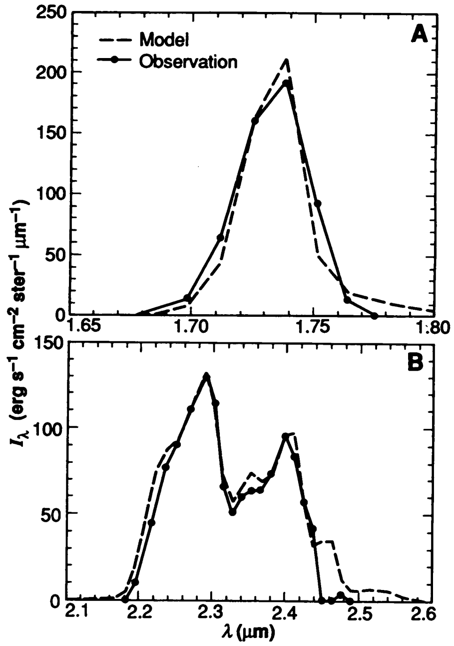

Fig. 8. Comparison of data and theoretical models for two spectral windows. In this paper, we have used only the 1.74- and 2.30-μm features to derive minor constituent abundances, but additional, altitude-dependent information is available from other short-wavelength windows. (**A**) Comparison of observations and model calculations within the 1.74-μm window, where we find an average water vapor mixing ratio of 50 parts per million by volume, probing the ~20-km region. The edges of this window are limited by CO_2 absorption, but the central value is determined by both water and CO_2 features. (**B**) The relatively broad 2.30-μm spectral feature that probes the ~30-km region and includes information on the 2-0 band of CO and water vapor abundances (in the long-wavelength slope), as well as OCS (*6*).

these species by comparing theoretical calculations to the observed spectra (*2, 3, 4, 6, 19*). Preliminary results for a few of the VJBARS spectra are presented below (we used the 1.74- and 2.30-μm windows). The width of the 1.74-μm feature is governed by CO_2 absorption, but its central intensity depends on the water vapor abundance at ~20 km, allowing an estimate for the H_2O mixing ratio in that altitude region. The 2.30-μm window is sensitive to CO, H_2O, and OCS in the ~30-km altitude region. Additional profile information, especially for water vapor, may be available in the shorter wavelength windows at 1.01, 1.09, 1.18, and 1.28 μm.

Figure 8 compares spectra with theoretical calculations for the two windows used. Details of the models used, the fitting procedures, and the spatial variability of the retrieved parameters will be given elsewhere (*20*), but one model was quite similar to that of Kamp *et al.* (*3, 4*) and a second (*19*) was a faster version that was based on a simplified radiative transfer scheme and band models, permitting rapid comparisons to the observations for a wide range of input parameters. In both models, we have used the new high-temperature CO_2 spectroscopic database of Wattson and Rothman (*21*) and the data of Rothman (*22*) to incorporate the numerous hot bands important for the conditions encountered in the Venusian lower atmosphere. The principal sources of uncertainty at present are (i) the presence of a poorly characterized pressure-induced CO_2 absorption in the 2.30-μm window which overlaps the CO and OCS bands (*23*), (ii) residual uncertainties in the strengths and far wing profiles of CO_2, (iii) the possible presence of SO_2 features and other unidentified absorbers, and (iv) minor corrections to the radiometric and wavelength calibration of the instrument. Among these categories, item (i) has by far the largest influence on the retrieved abundances, and further laboratory investigations are required to reduce the resulting uncertainty. Water vapor abundances have been retrieved as a result of fits in the two spectral windows, and the results are tabulated in Table 1. Although there is good agreement between the two different retrieval methods, the absolute abundances should be consid uncertain by a factor of 2 in this preliminary analysis. No attempt has been made to reconstruct a detailed vertical profile, but these measurements are sensitive to different depths in the atmosphere and suggest a variation of water vapor mixing ratio with altitude. Our results are in good agreement with ground-based observations (*2*) but are lower than Pioneer and Venera Probe measurements (*24*) by a factor of ~2 or more. A cursory examination of the water vapor abun-

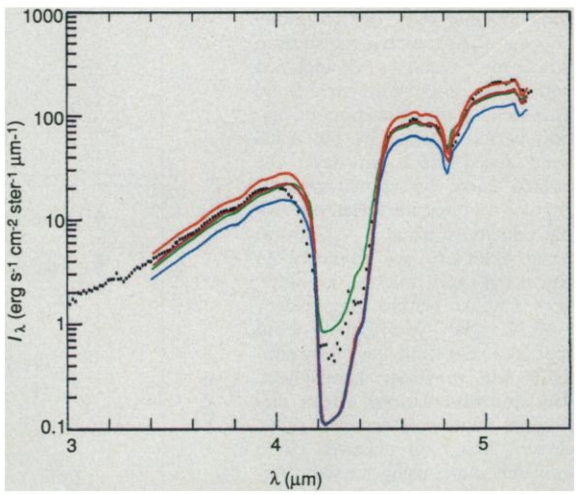

Fig. 9. Cloud and upper atmosphere thermal emission spectrum. This spectrum shows 3- to ~5-μm thermal emission that emanates from the clouds and, in regions of strong CO_2 opacity, from the atmosphere above. In general, the clouds radiate at a brightness temperature of ~235 K, but the detailed spectral shape depends on altitude variations in both temperature and cloud-atmosphere opacity. The shape of the spectrum can be used to investigate such vertical structure; in particular one can estimate the temperature lapse rate dT/dz and the cloud particle scale height H_c at the top of the upper cloud. In this figure we compare a center-of-disk VJBARS spectrum, shown as black points, with four model calculations that provides constraints for these quantities. The theoretical results are encoded as follows:

Color	Cloud temperature (K)	dT/dz (K km^{-1})	H_c (km)
Orange	235	−4.3	2.0
Red	230	−4.3	3.0
Green	230	−3.3	3.0
Blue	225	−4.3	5.0

Table 1. Minor constituent abundances derived from NIMS spectra.

Species	Spectral window (μm)	Approximate altitude (km)	Volume mixing ratio (parts per million)
H_2O*	2.30	30–35	25
	1.74	20–28	50
CO†	2.30	30	7–30
OCS‡	2.30	Tropospheric	0.2–1.0

*In this preliminary analysis we used only two bands for H_2O abundance determinations; additional information is available from shorter wavelength windows. The altitudes for our water vapor determinations were estimated by two methods. The first uses the height ($\pm$5 km) where changes in the water vapor mixing ratio produces the greatest change in signal; the second refers to the altitude corresponding to calculated brightness temperatures (in the absence of cloud extinction). The errors for the H_2O mixing ratio for this first analysis are conservatively estimated to be within a factor of 2, that is, +100% − 50%. †The primary uncertainty in the CO mixing ratio is the value of the CO_2 pressure-induced absorption coefficient and its spectral profile. ‡The OCS band may be overlapped by other absorption features of unknown origin [see (*6*) and text].

dance has shown no obvious latitudinal dependence, in contrast to the suggestion of Revercomb *et al.* [in (*24*)]. No significant correlation with cloud optical depth is apparent.

The retrieved CO abundances shown in Table 1 relate to a height range near 30 km. The abundance of this species is known to vary with altitude, because it is produced photochemically in the middle atmosphere. Our preliminary estimate is consistent with the profile derived from Pioneer Venus measurements (*25*) and the ground-based results of Bezard *et al.* (*6*) but is uncertain by as much as a factor of 4. The primary cause of this uncertainty is the lack of knowledge of the CO_2 pressure-induced absorption coefficient, which affects the spectral shape in the region of the CO 2-0 band. There are two estimates for the pressure-induced absorption coefficient (*23*), which differ by a factor of 3.5 and yield CO abundances differing by a factor of 2.5. As for H_2O, further study of the CO_2 feature in the laboratory will improve the accuracy of our results for Venusian CO in the future.

Although OCS features are not resolved in the NIMS measurements, they are known to be present and to affect the long-wavelength side of the 2.30-μm window (*6*). The current best retrieved value for OCS (Table 1) is very close to that obtained by Bezard *et al.* (*6*) from an analysis of the 2.30-μm feature obtained in high-resolution ground-based spectra. However, this region is also affected by the uncertain pressure-induced CO_2 absorption band, is overlapped by H_2O absorption features, and may contain additional absorbers; consequently, our interim value is uncertain by a factor of 5.

As a final note, we consider wavelengths greater than ~2.8 μm, for which the spectrum of Venus approximately follows a blackbody curve, corresponding to the temperature of the upper cloud, with CO_2 absorption bands superimposed at 4.25 μm (ν_3), 4.85 μm ($\nu_1 + \nu_2$), and 5.15 μm ($3\nu_2$). The CO_2 bands can be used to probe the thermal structure above the cloud level. As an example, Fig. 9 shows a typical center-of-disk NIMS spectrum compared to several models, in which the cloud altitude, the cloud scale height, and the temperature gradient above the cloud are chosen as free parameters. From this spectrum, a cloud scale height $H_c = 3^{+2}_{-1}$ km is derived, and a temperature gradient of $dT/dz = -4.3\ (\pm 1)$ K km^{-1} is found. These values are in good agreement with the combined product $F = (dT/dz)\ H_c$ derived from our VPDIN-1 center-to-limb variations based on the analysis method of Diner (*26*), from which we find $F = -11.8 \pm 0.5$ K km^{-1} km.

REFERENCES AND NOTES

1. D. A. Allen and J. W. Crawford, *Nature* **307**, 222 (1984); D. A. Allen, *Icarus* **69**, 221 (1986).
2. D. Crisp, D. A. Allen, D. H. Grinspoon, J. B. Pollack, *Science* **253**, 1538 (1991); see also *Int. Astron. Union Circ. 4962* (February 1990), wherein D. Allen reports new Venus features at 1.08 to 1.11, 1.17 to 1.20, 1.26 to 1.28, and 1.30 to 1.31 μm, observed from the Anglo-Australian Telescope.
3. L. W. Kamp, F. W. Taylor, S. B. Calcutt, *Nature* **336**, 360 (1988).
4. L. W. Kamp and F. W. Taylor, *Icarus* **86**, 510 (1990).
5. D. Crisp *et al.*, *Science* **246**, 506 (1989).
6. B. Bezard, C. de Bergh, D. Crisp, J.-P. Maillard, *Nature* **345**, 508 (1990).
7. A comprehensive description of the NIMS instrument will soon be published in R. Carlson *et al.*, *Space Sci. Rev.*; a brief description can be found in I. Aptaker, *SPIE J.* **834**, 196 (1987).
8. A. P. Ekonomov, Yu. Golovin, V. I. Moroz, B. E. Moshkin, in *Venus*, D. M. Hunten, L. Colin, T. M. Donahue, V. I. Moroz, Eds. (Univ. of Arizona Press, Tucson, 1983), pp. 632–649. See their figure 4, p. 639, showing low-altitude transmission spectra with maxima at 1.01, 1.09, and ~1.18 μm. These features correspond to some of the observed emission bands shown in our spectra (Fig. 1). Venera 11 also found high transmission for wavelengths less than 0.9 μm, and some portion of the short-wavelength intensities shown in Fig. 1 must arise from Venus atmospheric sources.
9. We have used the Venus topographic map prepared by the Massachusetts Institute of Technology and the U.S. Geological Survey, based on G. E. McGill *et al.*, in *Venus*, D. M. Hunten, L. Colin, T. M. Donahue, V. I. Moroz, Eds. (Univ. of Arizona Press, Tucson, 1983), pp. 69–130.
10. F. W. Taylor *et al.*, *J. Geophys. Res.* **85**, 7963 (1980); F. W. Taylor, D. M. Hunten, L. V. Ksanfomaliti, in *Venus*, D. M. Hunten, L. Colin, T. M. Donahue, V. I. Moroz, Eds. (Univ. of Arizona Press, Tucson, 1983), pp. 650–680.
11. The main cloud decks of Venus consist of sulfuric acid particles and are arranged in three contiguous layers within the altitudes of about 48 to 70 km. The upper cloud, which shows a base at ~57 km and a diffuse upper boundary, shows a bimodal size distribution, with mean modal diameters of 0.4 and 2.0 μm (termed modes 1 and 2). The middle cloud, occurring between 51 and 57 km, exhibits a trimodal distribution with particle diameters of ~0.3, 2.5, and 7.0 μm. In the lower cloud (~48 to 51 km), trimodal distributions are also found with corresponding sizes of ~0.4, 2.0, and 8.0 μm. The total optical depth of the clouds is ~30, with roughly equal contributions from the upper, middle, and lower clouds as well as from each of the three modes (to within a factor of ~3). See the review by L. W. Esposito, R. G. Knollenberg, M. Ya. Marov, O. B. Toon, R. P. Turco, in *Venus*, D. M. Hunten, L. Colin, T. M. Donahue, V. I. Moroz, Eds. (Univ. of Arizona Press, Tucson, 1983), pp. 484–564. We use a baseline cloud model suggested by Kamp and Taylor (*4*).
12. A. Sieff, in *Venus*, D. M. Hunten, L. Colin, T. M. Donahue, V. I. Moroz, Eds. (Univ. of Arizona Press, Tucson, 1983), pp. 215–279; V. S. Arduevskiy *et al.*, *ibid.*, pp. 280–298.
13. Prior spacecraft results for optical tracking of Venus zonal and meridional winds can be found for Mariner 10 in M. Belton, G. Smith, G. Schubert, and A. D. Del Genio [*J. Atmos. Sci.* **8**, 1394 (1976)] and for Pioneer Venus in S. S. Limaye and V. E. Soumi [*J. Atmos. Sci.* **38**, 1220 (1981)] and G. Schubert *et al.*, [*J. Geophys. Res.* **85**, 8007 (1980)]. A review is given by G. Schubert, in *Venus*, D. M. Hunten, L. Colin, T. M. Donahue, V. I. Moroz, Eds. (Univ. of Arizona Press, Tucson, 1983), pp. 681–765. Additional Galileo atmospheric velocity determinations are presented by M. J. S. Belton *et al.*, *Science* **253**, 1531 (1991).
14. C. C. Counselman, S. A. Gourevitch, R. W. King, G. B. Loriot, *J. Geophys. Res.* **85**, 8026 (1980).
15. D. Crisp, A. P. Ingersoll, C. E. Hildebrand, R. A. Preston, *Adv. Space Res.* **4**, 10 (no. 5), 109 (1990).
16. D. Crisp *et al.*, *Science* **253**, 1538 (1991).
17. For a discussion of multiple Hadley cells, see G. Schubert, in *Venus*, D. M. Hunten, L. Colin, T. M. Donahue, V. I. Moroz, Eds. (Univ. of Arizona Press, Tucson, 1983), pp. 681–765.
18. P. J. Schinder, P. J. Gierasch, S. S. Leroy, M. D. Smith, *J. Atmos. Sci.* **47**, 2037 (1990).
19. Th. Encrenaz, P. Drossart, E. Lellouch, in preparation; paper presented at COSPAR, The Hague, The Netherlands, May 1990.
20. R. W. Carlson *et al.*, in preparation.
21. This new high-temperature CO_2 data base uses accurate quantum-mechanical calculations to extrapolate line positions and strengths from existing experimental data. It supersedes the customary HITRAN database; see also R. B. Wattson and L. S. Rothman, *J. Mol. Spectrosc.* **119**, 83 (1986).
22. L. S. Rothman *et al.*, *Appl. Opt.* **26**, 4085 (1987).
23. There are two estimates for the absorption properties of the 2.30-μm CO_2 pressure-induced band. The first of these is contained in J. F. Moore, thesis, Columbia University (1971) [published in *NASA Techn. Mem. NASA-TM-X-65863* (1971)]. This suggests a wavelength-dependent absorption cross section with a peak value of 2×10^{-8} cm^{-1} amagat^{-2}. The second estimate was derived by Bezard *et al.* (*5*), using their high-resolution Venus spectrum, estimating a constant coefficient with a value of 7×10^{-8} cm^{-1} amagat^{-2}.
24. See V. I. Moroz [in *Venus*, D. M. Hunten, L. Colin, T. M. Donahue, V. I. Moroz, Eds. (Univ. of Arizona Press, Tucson, 1983), pp. 45–68] for a discussion of Venera spectrophotometer results. Pioneer Venus mass spectrometer data are presented in D. M. Hunten *et al.*, in *Origin and Evolution of Planetary and Satellite Atmospheres*, S. K. Atreya, J. B. Pollack, M. S. Mathews, Eds. (Univ. of Arizona Press, Tucson, 1989), pp. 386–426. Thermal net flux results are in H. E. Revercomb, L. A. Sromovsky, V. E. Soumi, *Icarus* **61**, 521 (1985).
25. For the CO distribution in the Venus atmosphere, see U. von Zahn, S. Kuhmar, H. Niemann, R. Prinn, in *Venus*, D. M. Hunten, L. Colin, T. M. Donahue, V. I. Moroz, Eds. (Univ. of Arizona Press, Tucson, 1983), pp. 299–430. In one analysis, we used an altitude-varying profile, following Kamp and Taylor (*4*). In a second determination we assumed a constant CO mixing ratio, but both determinations relate to the ~30-km formation level and the resulting estimates are quite similar, if allowance is

made for the uncertainty due to the poorly known CO_2 pressure-induced coefficient.
26. D. D. Diner, *J. Atmos. Sci.* **35**, 2536 (1979).
27. We thank the Galileo Project management and engineering staff for their continuing support of NIMS. We especially acknowledge the efforts of the late C. Yeates, Galileo Science and Mission Design Manager. We have lost a resourceful scientist and a good friend in his untimely death. We are grateful to N. Ausman, Galileo Mission Director, and the Orbiter Engineering Team for providing crucial real-time commands to the spacecraft during the Venus flyby. The Science Requirements and Operation Planning staff (J. Dunne, K. Buxbaum, and V. Henderson) formulated the highly successful Venus flyby sequences, providing us the opportunity to collect the data reported here. The preparation and processing of these data required the expertise of many people including J. Anderson, T. Arakelian, K. Becker, V. Carrere, R. Chang-Diaz, K. Edwards, E. Eliason, J. Gardner, M. Hernandez, S. Lavoie, F. Leader, R. Lopez-Gautier, C. Mahoney, R. Mehlman, M. Segura, J. Torson, L. Wainio, and J. Yoshimizu. We are grateful to B. Bezard, D. Crisp, D. Hunten, A. Lacis, and W. Rossow for valuable discussion and comments. This work was supported under NASA contract NAS 7-100 with the Jet Propulsion Laboratory, California Institute of Technology.

23 May 1991; accepted 19 August 1991

Galileo Ultraviolet Spectrometer Experiment: Initial Venus and Interplanetary Cruise Results

C. W. Hord, C. A. Barth, L. W. Esposito, W. E. McClintock, W. R. Pryor, K. E. Simmons, A. I. F. Stewart, G. E. Thomas, J. M. Ajello, A. L. Lane, R. W. West, B. R. Sandel, A. L. Broadfoot, D. M. Hunten, D. E. Shemansky

The Galileo Extreme Ultraviolet Spectrometer obtained a spectrum of Venus atmospheric emissions in the 55.0- to 125.0-nanometer (nm) wavelength region. Emissions of helium (58.4 nm), ionized atomic oxygen (83.4 nm), and atomic hydrogen (121.6 nm), as well as a blended spectral feature of atomic hydrogen (Lyman-β) and atomic oxygen (102.5 nm), were observed at 3.5-nm resolution. During the Galileo spacecraft cruise from Venus to Earth, Lyman-α emission from solar system atomic hydrogen (121.6 nm) was measured. The dominant source of the Lyman-α emission is atomic hydrogen from the interstellar medium. A model of Galileo observations at solar maximum indicates a decrease in the solar Lyman-α flux near the solar poles. A strong day-to-day variation also occurs with the 27-day periodicity of the rotation of the sun.

On 8 February 1990 the Extreme Ultraviolet Spectrometer (EUV) on the Galileo spacecraft obtained a spectrum of Venus in the wavelength range of 55 to 125 nm. After this encounter, the interplanetary cruise period from Venus in February 1990 to Earth in December 1990 was used for observations of atomic hydrogen Lyman-α (121.6-nm) radiation from the interplanetary medium. The EUV (*1*) has a mechanical collimator and a single-reflection Wadsworth optical system that uses a concave grating to feed a 128-pixel, bare microchannel plate detector. The resulting spectra have 3.5-nm spectral resolution for objects that fill the 0.87° by 0.17° field of view of the instrument. The spacecraft spin axis maintains an orientation that is within a few degrees of the sun while it is inside 1 astronomical unit (AU).

C. W. Hord, C. A. Barth, L. W. Esposito, W. E. McClintock, W. R. Pryor, K. E. Simmons, A. I. F. Stewart, G. E. Thomas, Laboratory for Atmospheric and Space Physics, University of Colorado, Boulder, CO 80309.
J. M. Ajello, A. L. Lane, R. W. West, Jet Propulsion Laboratory, California Institute of Technology, Pasadena, CA 91109.
B. R. Sandel, A. L. Broadfoot, D. M. Hunten, D. E. Shemansky, Lunar and Planetary Laboratory, University of Arizona, Tucson, AZ 85721.

The EUV is mounted on the spinning section of the spacecraft, and its field of view sweeps out a great circle 0.87° wide on the celestial sphere at about 3 rpm, passing through the north and south ecliptic poles in a plane perpendicular to the spacecraft spin axis. Commands to the EUV determine the fraction of the great circle observed and the number of bins (called sectors) into which that fraction is divided. During the Venus encounter individual photon events, together with a wavelength and a sky sector location, were stored on the spacecraft tape recorder for later playback to Earth. During the interplanetary cruise the photon events were integrated in the onboard memory of the EUV in a matrix of sector and wavelength knowledge, which was periodically read out.

During the Venus encounter EUV data were recorded for 75 min, 25 min of which contain the planet. The observed great circle was divided into 120 1.6° sectors: Venus filled 17 sky sectors as the spacecraft flew past at 22,000 to 29,000 km from the planet center. The disk-integrated dayglow spectrum of Venus (Fig. 1) shows several well-resolved emission lines. The feature at 121.6 nm (H Lyman-α) is due to resonance scattering of sunlight by atomic hydrogen. The feature near 102.6 nm contains H Lyman-β (102.57 nm) formed by resonance scattering and may contain a contribution from O pumped by the solar Lyman-β line, as occurs in the dayglow of Earth (*2*). The EUV brightness ratio of Lyman-α to the feature at 102.6 nm on Venus is 170, compared to the ratio of 624 measured by the EUV in the interplanetary hydrogen background. Also visible are lines of He (58.4 nm) and O^+ (83.4 nm), confirming earlier reported detections made with EUV instruments on Mariner 10 (*3*) and Venera 11 and 12 (*4*). The He line at 58.4 nm is due to resonance scattering of sunlight by atomic He. Several mechanisms can contribute to the formation of O^+ at 83.4 nm: direct photoionization excitation of atomic oxygen, electron impact ionization and excitation of atomic oxygen, and resonance scattering of sunlight by oxygen ions (*5*).

Other Venus emissions were observed in the region from 90 to 120 nm (Fig. 1); they are presumably an unresolved blend of several atomic or molecular emissions or both. The dayglow of Earth contains numerous oxygen and nitrogen emissions in this region (*5*). The strongest unresolved line in the Venus EUV spectrum is probably O (98.9 nm), prominent in the dayglow of Earth, (*6*) where it is excited by photoelectron impact (*5*). Table 1 indicates the derived brightnesses for the resolved and nearly resolved lines and compares the values to ones obtained with EUV instruments on Mariner 10 (*3*) and Venera 11 and 12 (*4*). Galileo brightness values represent the averages over the portion of the sunlit disk viewed by the instrument, whereas Mariner and Venera brightness values represent the largest value seen on the planet. Error estimates for the Galileo data are based on the uncertainties in the absolute calibration of the EUV in the laboratory.

For the Lyman-α measurements made during the interplanetary cruise period, the great circle swept out by the EUV sampled

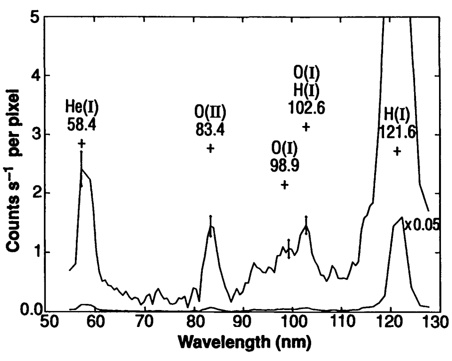

Fig. 1. The EUV spectrum of Venus. Error bars (±1 σ) have been placed on identified lines.